RSC Advances

PAPER

View Article Online
View Journal | View Issue



Cite this: *RSC Adv.*, 2020, **10**, 3105

# Modified top-down approach for synthesis of molybdenum oxide quantum dots: sonication induced chemical etching of thin films

Dibya Jyoti Borah,[a] Abu Talat Tahir Mostako, *[a] Angshuman Thunder Borgogoi,[a] Prasanta Kumar Saikia[b] and Ashim Malakar[c]

Received 22nd November 2019
Accepted 10th January 2020

DOI: 10.1039/c9ra09773b

rsc.li/rsc-advances

A simple and modified top-down approach to synthesize molybdenum oxide ($MoO_x$: $x = 2, 3$) quantum dots (QDs) is proposed in this study. This modified approach involves the conversion of a bulk powder material into thin films followed by a sonication induced chemical etching process for synthesising QDs. X-Ray Diffraction (XRD) is used for crystal structural characterization of $MoO_x$ thin films. The crystal structure properties of the $MoO_x$ QDs are analysed by High Resolution Transmission Electron Microscopy (HRTEM) images and corresponding Selected Area Electron Diffraction (SAED) patterns. The optical band gap is estimated by Tauc's plot from UV-Vis-NIR absorption spectra. The excitation dependent photoluminescence (PL) emission of $MoO_x$ QDs as a function of acid concentration is investigated. The growth mechanism of QDs in different crystalline phases as a function of acid concentration is also exemplified in this work. The micro-Raman and Fourier Transform of Infrared (FTIR) spectra are recorded to analyse the vibrational spectrum of the molybdenum–oxygen (Mo–O) bonds in the $MoO_x$ QDs.



## Introduction

Transition Metal Oxide (TMO) nanostructures have shown great promise and are being investigated with great attention for basic scientific and industrial research owing to their unique physical and chemical properties.[1–3] Among TMOs, molybdenum oxide ($MoO_x$) based nano-materials with different morphologies have attracted great attention in recent years due to their optical, electronic, and structural features.[4–13] One dimensional (1D) and two dimensional (2D) nano-belts,[4,5] nano-rods,[3,6] nano-wires,[7,8] nano-flowers,[9] nano-ribbons,[10] nano-sheets,[11,12] and nano-films[13] have stimulated great research interest in recent years. $MoO_x$ nano-materials have been pioneering through their uses in solar cells,[14,15] lithium ion batteries,[16,17] field effect transistors,[18] gas sensors,[19] antiseptics and anticancer treatment.[20,21] Zero dimensional $MoO_x$ QDs exhibit enhanced optical and electronic properties due to the quantum confinement effect, which originates from their small size (~10 nm) compared to their 1D or 2D morphology.[22–24] Low toxicity, superior photostability, biocompatibility and excellent chemical stability, enables $MoO_x$ QDs a potential candidate for metal ion sensing, small biomolecule detection, biological labelling and imaging.[25] Moreover, oxygen deficient $MoO_{3-x}$ ($2 < x < 3$) QDs used for photothermal ablation of cancer cells due to strong near infrared (NIR) absorption and high photothermal conversion efficiency.[26,27] $MoO_x$ QDs containing in solution phase of hydrochloric acid (HCl) have a potential application in photothermal treatment and biological sensing due to low cost production and high sensitivity.[26,27] This solution phase of QDs are also applied in rapid colorimetric detection of glucose.[26] $MoO_x$ nano-materials can be well extracted from its solution phase. T. T. P. Pham *et al.* reported that the heat treatment at elevated temperature ~150 °C for 1 hour duration eliminates HCl acid and water from the solution containing $MoO_x$, and are able to extract $MoO_x$ nano-materials in powder form.[28] As received powder of $MoO_x$ nano-materials exhibited excellent catalytic properties in partial oxidation of methanol to formaldehyde.[28] As an advance branch of low dimensional materials, 2D QDs derived from atomically-thin 2D sheets *viz*; graphene, transition metal dichalcogenide, graphitic carbon nitride, hexagonal boron nitride, and phosphorene, are emerging extraordinary low dimensional materials.[23,29] The 2D QDs have wide range of applications including bio-imaging, photo-induced therapy, chemical and metal ion sensors, and photovoltaic devices.[23,29]

Generally, the synthesis of $MoO_x$ QDs can be classified in two approaches: top-down and bottom-up method.[26,30] Top-down approach mainly relies on weakening the van der Waals interaction between adjacent layers and breaking the strong covalent bonding within each layer to exfoliate the structure or bulk

[a]*Material Science Laboratory, Department of Physics, Dibrugarh University, Dibrugarh-786004, Assam, India. E-mail: mostako@dibru.ac.in; abumostako@gmail.com*

[b]*Thin Film Laboratory, Department of Physics, Dibrugarh University, Dibrugarh-786004, Assam, India*

[c]*Central Instrumental Facility, Indian Institute of Technology Guwahati, Guwahati-39, India*

materials.[26,31] Alternatively, QDs of layered materials prepared by a top-down approach do not require an insulating ligand coating, which is deleterious to electrical transport of the materials, especially in the application of catalysis and electronics.[22,31] Top-down approaches, such as laser ablation,[32] e-beam lithography,[33] can be used to reduce the particle size. Unfortunately, such methods are weakly feasible for the high yield preparation of QDs in solution phase and are also restricted due to the need of extremely expensive instrumental facilities. QDs synthesis by bottom-up approaches, suffer from insulating ligand coating, which affect the electrical transport of properties of the material.[31] In the meantime, Huang *et al.* reported that $MoO_{3-x}$ nanotubes have been successfully synthesized *via* hydrothermal method in presence of thiol by means of bioligand and surfactant.[34] However, the poor hydrophilicity of the resulting products owing to the difficulties experienced for complete removal the surfactant or organic ligand molecules. A combination of sonication and solvothermal treatment of bulk $MoS_2/WS_2$ was used by Xu *et al.* for $MoS_2/WS_2$ QDs synthesis.[35] But, requirement of high temperature and frequent sonication resulted breaking of bulk crystals down to nano-sheets indicates further refinement.[36,37] Difficulties persisted in the existing synthesis procedure of TMO QDs as per present literature survey depicts the need of alternative approach for the synthesis without any incongruities. Therefore, in this manuscript a simple and modified top-down method is proposed for synthesis of $MoO_x$ QDs. This method is a combination of thermal evaporation and sonication induced chemical etching process. Every synthesis method needs a careful optimization of various parameters involved in that method. Sonication is an effective tool that can avoids the formation of large clusters and aggregation of $MoO_3$ nanoparticles. Sonication frequency, duration and temperature of the sonication bath has a vital role on the growth process of QDs. S. Bai *et al.* and Z. Wu *et al.* have reported that the increase in sonication duration produces more smother and regular particles with better crystallinity.[19,38] Keeping these in mind, at fixed sonication duration and sonication temperature, the effect of parametric variation of etchant concentration on the synthesis and their effect on the optical and structural properties of $MoO_x$ QDs is investigated in the present work.

## Experimental section

### Materials and reagents

Molybdenum(VI) oxide powder (Sigma-Aldrich, 99.97% purity) was used as source material. Hydrochloric acid (Emplura®, ≥ 35%), nitric acid (Emplura®, 68–70%) and acetone (Emplura®, ≥ 99.0%) were of analytical grade and used without further purification. Glass microscope slides (76.2 mm × 25.4 mm × 1.2 mm) were used as substrates for thin film fabrication. Throughout all the experiments, deionized water was used.

### Synthesis of $MoO_x$ QDs

$MoO_x$ QDs were synthesized from molybdenum oxide powder in two step process. In the first step: an amount of 0.1 g molybdenum(VI) oxide powder is evaporated from molybdenum boat by supplying a current ~3.0–3.4 A in a thermal evaporation setup (Model: HINDHIVAC 12″ vacuum coating unit, 12A4D). The duration of deposition is ~10 min. $MoO_x$ films are deposited on clean glass substrate (5.52 cm × 2.54 cm) by thermal evaporation technique at substrate temperature ~100 °C and base pressure ~$2 \times 10^{-5}$ torr. Prior to thin film deposition, the glass substrates were cleaned by usual cleaning protocols as described in our previous work.[39] The second step depicts the chemical etching of as-deposited $MoO_x$ thin films. Prior to chemical etching, a 4 mL 25% diluted hydrochloric acid (HCl) was prepared in a glass breaker of 10 mL. This 4 mL solution was prepared by mixing 3 mL concentrated HCl (~35%) and 1 mL deionized water. During the process of chemical etching, the breaker containing the mixture solution and submerged film in it, was partially dip into the water bath of the sonicator and continuously sonicated with frequency ~50 Hz for 30 minutes. The temperature of the water bath was maintained at 45 °C. After that, a light yellow colour solution is obtained. In this work, two samples are prepared by changing the concentration of HCl acid from 25% to 30%. The samples are coded as $S_1$ and $S_2$, respectively.

### Characterizations

The crystal structural properties of $MoO_x$ film is characterized by XRD (Model: Rigaku Ultima (IV)), using Cu-$K_\alpha$ monochromatic radiation ($\lambda = 1.541$ Å) with a potential of 40 kV and current of 30 mA. The $2\theta$ angle of the detector was scanned typically in between 10° and 70° with a step size of 0.15°. The size of $MoO_x$ particles are investigated by field emission transmission electron microscope (Model: JEOL 2100F) image analysis, operated with an acceleration voltage of electron beam ~200 kV. HRTEM images were captured to observe the nanoparticle formation while the SAED pattern were recorded for analysing the modification in crystalline structure of the QDs as a function of HCl acid concentration. The average particle size and lattice spacing are estimated from fringing pattern in the HRTEM images by using Gatan Digital Micrograph software. For spectroscopic analysis, the absorption, fluorescence, Raman and FTIR spectra of the $MoO_x$ QDs are recorded. Absorption spectra are recorded by using a UV-Vis-NIR Spectrophotometer (Model: Shimadzu UV-3101 PC) in wavelength range, 200–3000 nm with an interval of 1 nm. The optical band gap of $MoO_x$ QDs is calculated from absorption spectra by using Tauc's plots. Fluorescence spectra of QDs are recorded by using a Spectrophotometer (Model: Horiba Scientific Fluoromax-4 Spectrofluorometer) at different excitation wavelengths 260, 270, 300, 320, 350 nm and 280, 300, 320, 350, 380 nm, for the sample $S_1$ and $S_2$, respectively. Raman spectra of the QDs were recorded at room temperature using laser micro-Raman setup (Model: Horiba Jobin Vyon, Lab-Ram HR 800) under 532 nm wavelength as an excitation source. Fourier Transform Infrared (FTIR) absorption spectra are recorded by FTIR Spectrometer (Model: PerkinElmer (BX)) to study the bonding nature of Mo–O in the $MoO_x$ QDs. For FTIR studies, a small amount of sample solution was dried onto silicon substrate.

 

## Results and discussion

### Crystal structure and particle size analysis

The synthesis procedure of $MoO_x$ QDs from bulk molybdenum oxide powder is shown schematically in Fig. 1. Thermally deposited $MoO_x$ layers are etching slowly into small particles. These particles further fragmented to even more small particles by ultra-sonication, which lead to the formation of well dispersed $MoO_x$ QDs. The $MoO_x$ thin films are deposited on glass substrate at 6 cm source-substrate distance and room temperature. The XRD spectrum of bare glass and thermally deposited $MoO_x$ thin film are shown in Fig. 2.

The broad XRD peak ranging from $2\theta \sim 20°$ to 30° is observed in the $MoO_x$ film due to the glass substrate only. No significant XRD peaks are observed in the $MoO_x$ film. This may be attributed to the low mobility of evaporated atoms on the substrate surface and less interaction between the molybdenum and oxygen since this film is deposited at room temperature.[39] Similar thin film samples are prepared under same deposition parameters that are subjected to chemical etching process for synthesis of QDs.

FETEM image analysis is carried out to investigate the size of the particles and crystallographic orientation of prepared QDs. FETEM image of the sample $S_1$ is shown in Fig. 3(a). It confirmed the formation of nearly spherical shape of $MoO_x$ QDs of sample $S_1$. The size distribution histogram gives the average size among thirty QDs is ~4.3 nm, shown in Fig. 3(b) for the sample $S_1$. The Fig. 3(c) shows the bright field image of corresponding SAED pattern. The SAED pattern revealed that QDs are polycrystalline in nature. There are two lattice planes each (218) and (420) corresponding to h-$MoO_3$ phase (JCPDS: 21-0569) and that of (200) and (060) corresponding to α-$MoO_3$ phase (JCPDS: 05-0508), respectively. The HRTEM images, Fig. 4(a)–(d) reveals that lattice spacing of QDs are ~0.20 nm correspond to (320) lattice plane of h-$MoO_3$ phase (JCPDS: 21-0569) and ~0.22 nm, 0.23 nm and 0.19 nm correspond to (150), (060) and (200) lattice planes of α-$MoO_3$ phase (JCPDS: 05-0508), respectively.

Moreover, FETEM image confirmed the nearly spherical shape of $MoO_x$ QDs for the sample $S_2$, as shown in Fig. 5(a)–(d). The size distribution histogram gives the average size ~4.6 nm (Fig. 5(b)). The SAED pattern, Fig. 5(c), revealed that these QDs are also polycrystalline in nature. Highly ordered and parallel

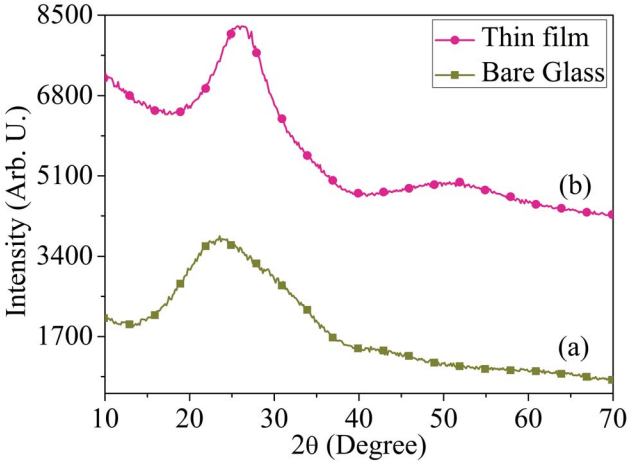


Fig. 2 XRD spectrum of (a) bare glass and (b) thermally deposited $MoO_x$ thin film, respectively.

lattices in the HRTEM image, Fig. 5(d) of the QDs suggested its crystallization with lattice spacing ~0.26 nm, which is associated with (140) lattice plane of α-$MoO_3$ phase (JCPDS: 05-0508). For the samples: $S_1$ and $S_2$, the inter planner spacing along with crystal planes observed in HRTEM image and estimated from SAED pattern are listed in Table 1. These studies indicate that the small nano-crystals are QDs of $MoO_3$. The bulk $MoO_3$ powder can be transformed to the QDs with tuneable phase and size with the careful optimization of various parameters involved in this modified technique. In addition, by this modified technique amorphous $MoO_x$ thin film is successfully transformed into the polycrystalline QDs with co-existence of α-$MoO_3$ and h-$MoO_3$ phase, as confirmed by XRD and SAED patterns analysis. There are several reports on the synthesis of $MoO_x$ nano-materials in presence of surfactant.[4,19,40] However, in the present work a well dispersed stable $MoO_x$ QDs are successfully synthesized without any surfactant. The observed polydispersity of the particle size distribution can be minimized with the use of suitable capping or stabilizing agent during the chemical etching process.

The increase of size of the particles with the increase of solution concentration (more than two sample concentration) were reported by H. S. Dehsari *et al.* and J. H. Huang *et al.*[41,42] In

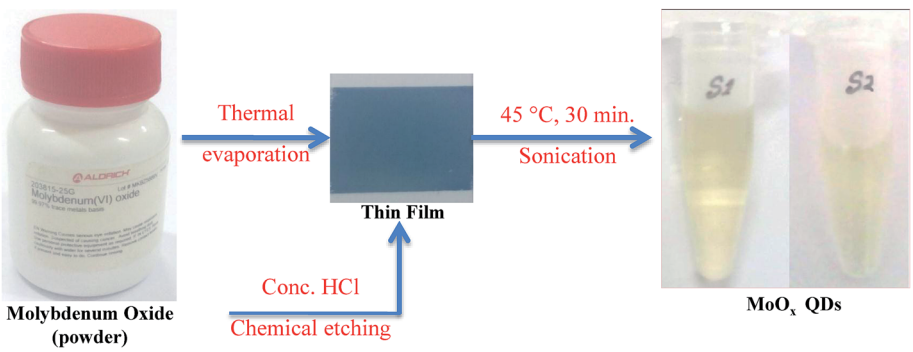


Fig. 1 Schematic representation of synthesis of $MoO_x$ QDs from bulk molybdenum oxide powder.

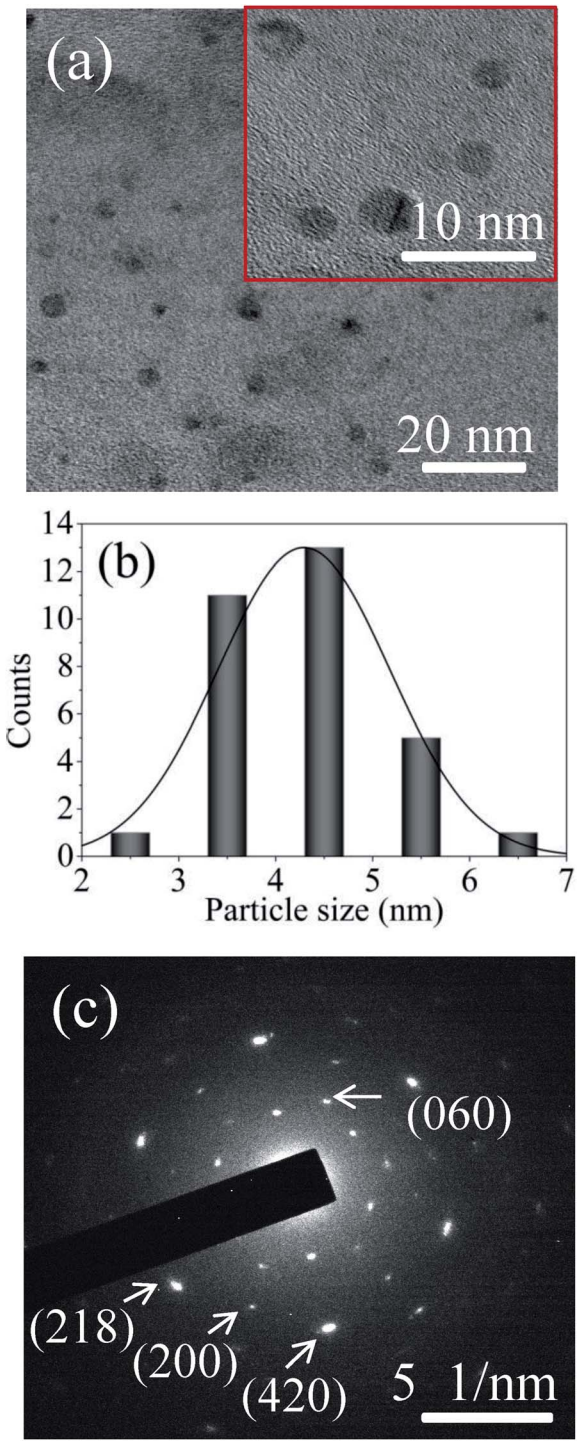


Fig. 3 (a) FETEM image of the sample $S_1$ (inset magnified area), (b) the corresponding particle size distribution histogram, and (c) SAED pattern of $MoO_x$ QDs for the sample $S_1$.

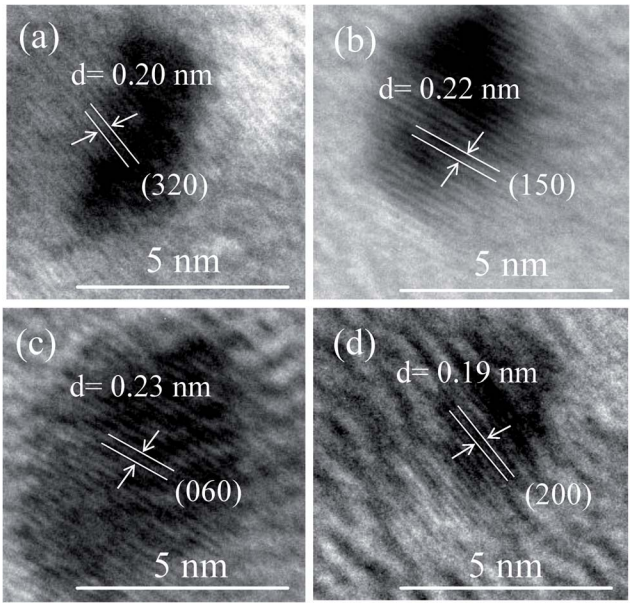


Fig. 4 (a–d) The HRTEM image of four different $MoO_x$ QDs of the sample $S_1$.

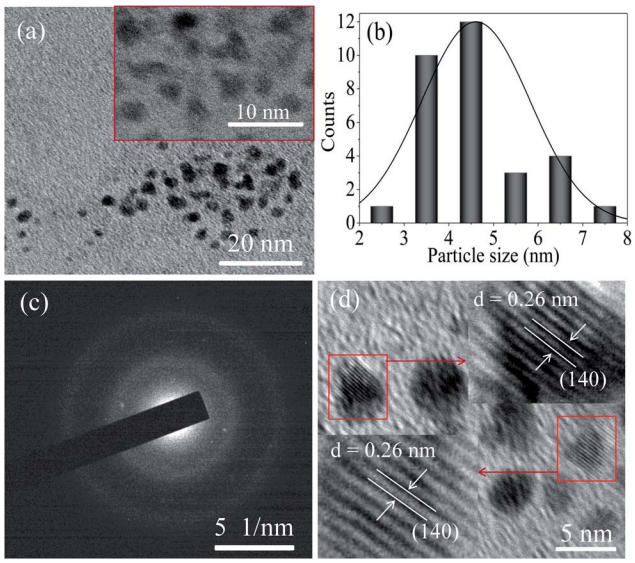


Fig. 5 (a) FETEM image of the sample $S_2$ (inset magnified area), (b) the corresponding particle size distribution histogram, (c) the SAED pattern of $MoO_x$ QDs, and (d) the HRTEM image of $MoO_x$ QDs for the sample $S_2$.

the present investigation, similar increase in the size of QDs with the increase in HCl acid concentration in the sample solution is also observed. It is because, only few particles are available at the lower concentration of the solution and they tend to stay apart due to strong repulsive force. This reduces the growth rate due to less mass transfer in the reaction medium.[41,42] However, at higher concentration the number density of the particles is increased which in turn reduced the inter-particle distances. There is a high mass transfer at low inter-particle distance and thereby causing the higher growth rate of the QDs.[41,42] The QDs are synthesised at lower HCl acid concentration showed the co-existence of h-$MoO_3$ and $\alpha$-$MoO_3$ phases. It is also observed that these mixed phase transformed to thermodynamically stable $\alpha$-$MoO_3$ phase with increase of HCl acid concentration from 25% to 30% in the solution. It is

 

Table 1 Estimated optical and structural parameters of $MoO_x$ QDs along with the sample codes

| Sample code | Concentration of HCl acid (%) | Band gap energy (eV) | Average particle size (nm) | Inter planner spacing, $d$ (nm) | ($hkl$) planes | Phase assignment |
|---|---|---|---|---|---|---|
| $S_1$ | 25 | ~5.01 | ~4.3 | 0.20 | (320) | h-$MoO_3$ |
| | | | | 0.22 | (150) | h-$MoO_3$ |
| | | | | 0.23 | (060) | α-$MoO_3$ |
| | | | | 0.19 | (200) | α-$MoO_3$ |
| $S_2$ | 30 | ~4.98 | ~4.6 | 0.26 | (140) | α-$MoO_3$ |
| | | | | 0.26 | (140) | α-$MoO_3$ |

because, at lower concentration of HCl acid, only few $H^+$ ions were adsorbed on the negative polar plane of growth unit of the $MoO_3$ *i.e.*, $MoO_6$ octahedron. Thus, the corner to corner growth became the basis of the growth unit and it easily developed into a network shaped h-$MoO_3$ phase.[43] With the increase of HCl acid concentration in the sample solution, the concentration of $H^+$ ion increased, which play a crucial role in $MoO_3$ phase transformation. The growth rate of the negative polar plane of $MoO_6$ octahedron is blocked, due to more and more $H^+$ ions were adsorbed at the negative polar plane. Instead, the growth rate of the positive polar plane of $MoO_6$ octahedron was far greater than others. Therefore, the growth is changed to superposition by sharing the edges and by sharing the corners of the positive polar plane structure, which developed into an α-$MoO_3$ phase.[43] In addition, the lower concentration of HCl acid will favour the formation of h-$MoO_3$ phase.[44]

## Spectral analysis

**Absorption characteristics.** The UV-Vis absorption spectra of $MoO_x$ QDs in the wavelength range, 200–400 nm for different concentration of HCl acid as shown in Fig. 6. The spectra confirm that the as-prepared $MoO_x$ QDs shows characteristic UV-Vis absorption peak at ~219 nm and strong absorption between 200-300 nm. The strong absorption is due to the charge transfer of Mo–O band in the $MoO_6^{6-}$ octrahadron.[40,45] The broadening of the absorption peak is ~22 nm and ~23 nm for the sample $S_1$ and $S_2$, respectively. The change in full width at half-maximum (FWHM) broadening with the change in HCl acid concentration 25% to 30% is observed to be marginal. The narrow FWHM data of QDs reflects their smaller particle size distribution.[46,47] This is consistent with the present findings. The light yellow colour of the solution of $MoO_x$ QDs, as shown in Fig. 1, confirmed the formation of molybdenum trioxide ($MoO_3$).[26,48,49] The absence of distinct precipitation of the yellow solution indicates the fine disparity and stability of $MoO_x$ QDs. The absorbance is increased to ~1.2 for sample $S_2$ in comparison to that of $S_1$, ~0.9 along with bathchromic shift of ~8 nm at the wavelength 230 nm. Higher HCl acid concentration in sample $S_2$ produces more number of particles in the solution. This in turn led to the increase in absorbance. In addition, the red shift of absorption edge of sample $S_2$ in comparison to that of $S_1$ indicates the increase of particle size, which is in accordance with the result obtained from FETEM characterization. The optical band gaps ($E_g$) of QDs in the present work are estimated by using the eqn (1),[50,51]

$$\alpha h\nu = B(h\nu - E_g)^m \quad (1)$$

where, '$B$' is the Tauc's slope, '$h\nu$' is the photon energy, '$m$' is the transition probability. The value of '$m$' is $\frac{1}{2}$ for allowed transition in direct band gap material.[50,51] The $(\alpha h\nu)^2$–$h\nu$ plot for both sample: $S_1$ and $S_2$, as shown in Fig. 7. The optical band gap is estimated by linear extrapolation of the $(\alpha h\nu)^2$–$h\nu$ plot. The

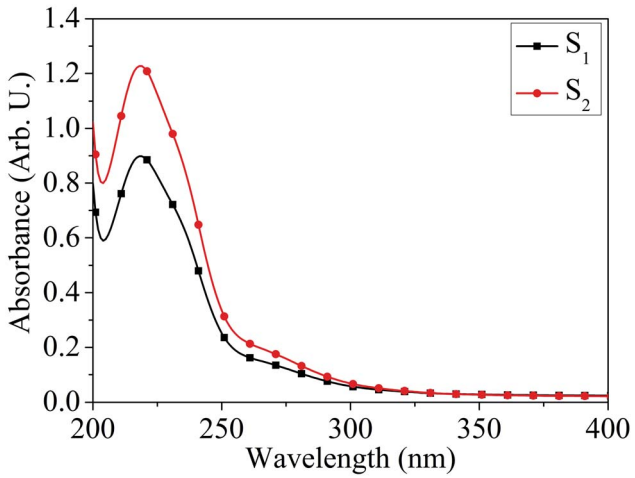


Fig. 6 UV-Vis absorption spectra of $MoO_x$ QDs for the samples: $S_1$ and $S_2$.

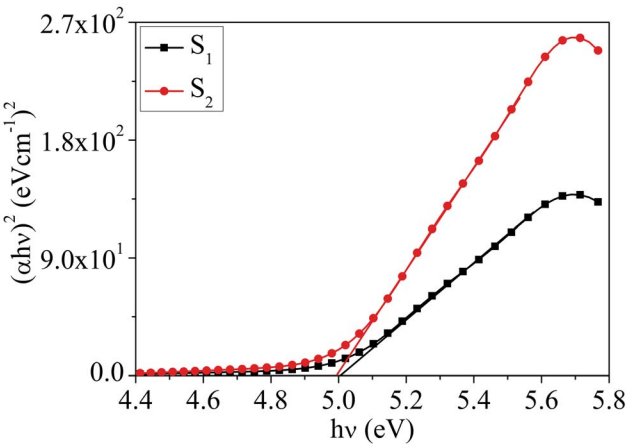


Fig. 7 The plot of $(\alpha h\nu)^2$–$h\nu$ for the samples: $S_1$ and $S_2$.

calculated values of band gap are listed in Table 1. The optical band gap of the samples: $S_1$ and $S_2$ are ~5.01 eV and 4.98 eV, respectively. The change is optical band gap is marginal with the present change in acid concentration. The band gap energy estimation shows there is blue shift for the $MoO_x$ QDs compared to that of bulk $MoO_3$ (~2.9 eV). This blue shift is due to the quantum confinement effect and hence, it reconfirmed the formation of QDs.[52,53] The histogram of band gap and average particle size of $MoO_x$ QDs for different acid concentration is shown in Fig. 8.

**Photoluminescence (PL) characteristics.** Time resolved PL was measured by a Life Spec-II, Edinburgh Instruments. The fluorescence decay curve of the sample $S_2$ is shown in Fig. 9(a). The residual counts of the fluorescence decay curve is shown in Fig. 9(b). A 308 nm LED from Pico Quant was employed as the excitation source with a Hamamatsu Micro Channel Plate (MCP) as the detector. Using the FAST software provided by Edinburgh Instruments Ltd, the fluorescence decays were analysed by the reconvolution method. The goodness of fit is determined by the reduced chi-square ($\chi^2$) values and weighted residuals. The fluorescence decay of both the samples: $S_1$ and $S_2$ show lifetime of 1.40 and 1.42 ns, respectively and listed in Table 2. These results are quite indicative of the fact that the PL emissions of the QDs are fluorescent in nature. The fluorescence decay of the sample $S_1$ and $S_2$ show a single exponential decay as suggested by good $\chi^2$ values.

The PL spectra of $MoO_x$ QDs for the samples: $S_1$ and $S_2$ shown in Fig. 10(a) and (b), respectively. Similar to that of nanoparticles, $MoO_x$ QDs also exhibit excitation dependent PL behaviour. For the sample $S_1$, PL spectra of $MoO_x$ QDs exhibit a strong emission peak at ~360 nm under an excitation wavelength 300 nm. This fluorescence emission peak at ~360 nm is due to the band to band transition and oxygen vacancies, Mo interstitial and surface defect of $MoO_x$ QDs. In addition, the emission peak at ~363 nm is related to the indigo emission corresponding to the near band edge emission and it is close to the reported value of 365 nm.[54,55] Similarly for the sample $S_2$, the strong fluorescence emission peak appears at ~410 nm upon excitation with 350 nm wavelength. As per crystal field model,

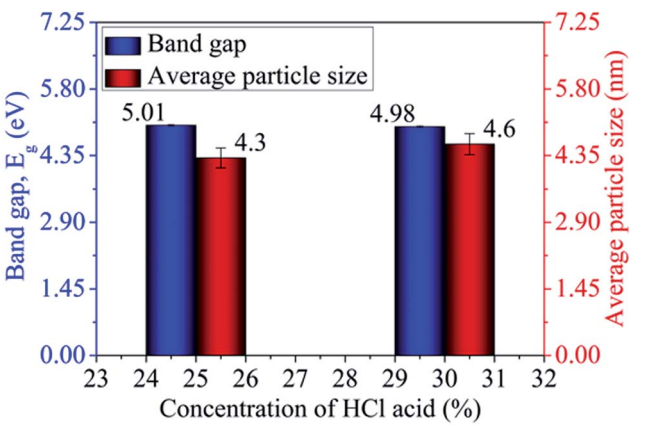


Fig. 8 Histogram of band gap and average particle size of $MoO_x$ QDs for different concentration of HCl acid.

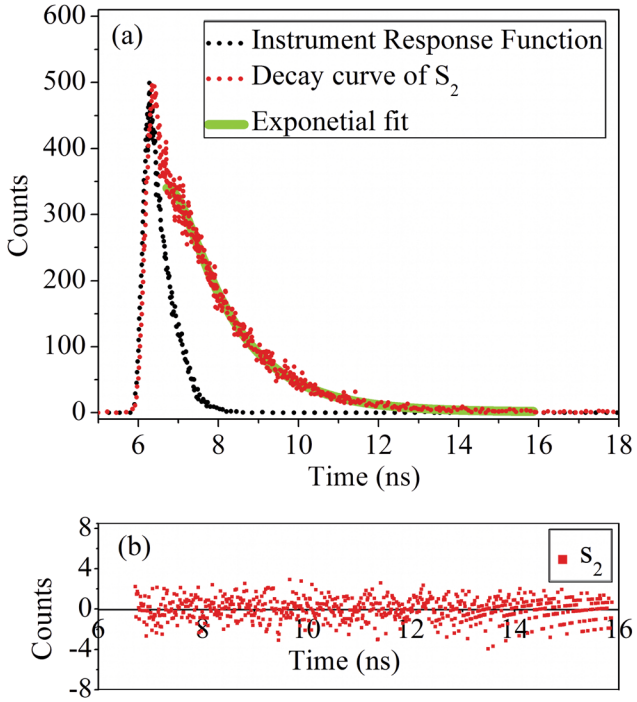


Fig. 9 (a) Fluorescence decay curve and (b) corresponding residual plot of the sample $S_2$.

the fluorescence emission peak at ~410 nm may be attributed due to the $Mo^{5+}$ $d_{yz^1}$–$d_{xy^1}$ band transition of a heavily distorted polyhedron (Mo–O) in a octahedral crystal field.[52] The blue emission peaks at ~420 and 400 nm are mostly related to the band to band transition with high Stokes shift.[56–58] Digging more into this experiment, PL spectra for both the samples were recorded at various excitation wavelengths. In these PL spectra, a very weak shoulders along with the strong fluorescence emission peaks are detected for both samples under different excitation wavelengths. The weak shoulders are appeared due to the electron–hole recombination between the conduction band and the sublevel of adsorbed oxygen acceptors; which are disappeared with the increase in excitation wavelengths.[59] The fluorescence emission peaks bathochromically shifted from ~363 to 360 nm for the sample $S_1$ with an increase in the excitation wavelength from 260 to 350 nm. The fluorescence intensity was observed to change with excitation wavelengths. Similar bathochromic shift from ~420 to 410 nm was also observed for the sample $S_2$ with the change in excitation wavelength from 280 to 380 nm. This phenomenon usually appears in QDs that derived from 2D materials.[40,60–63] This is because of

Table 2 Fluorescence lifetimes of $MoO_x$ QDs along with the sample codes

| Fluorophore | Monitoring $\lambda_{max}$ | Lifetime (ns) | $\chi^2$ |
|---|---|---|---|
| $S_1$ | 360 nm | 1.40 | 1.06 |
| $S_2$ | 360 nm | 1.42 | 1.05 |

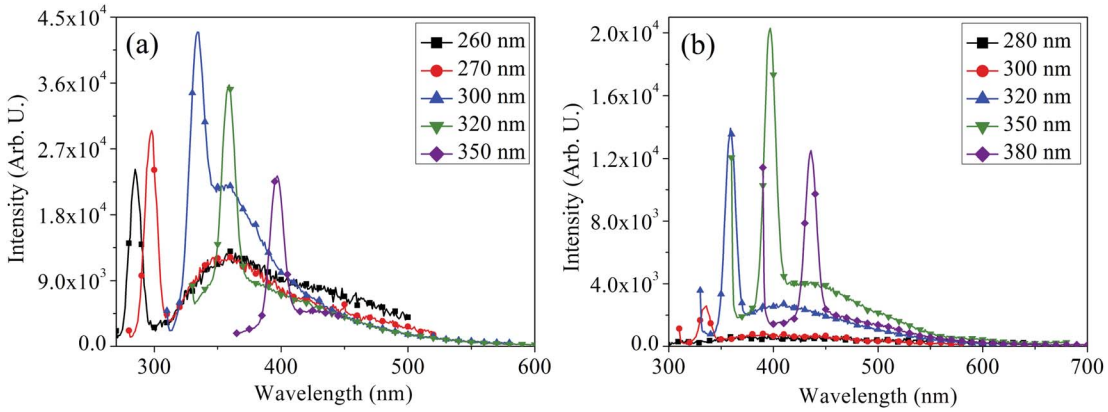


Fig. 10 Excitation dependent PL spectra of $MoO_x$ QDs for the samples (a) $S_1$ and (b) $S_2$, respectively.

the inhomogeneity of chemical components and polydispersity of the lateral sizes,[64] which is again in consistent with FETEM observation. This phenomenon mostly likely due to the distribution of emissive trap sites on the surface of $MoO_x$ QDs and quantum confinement effect.[60]

**Micro-Raman characteristics.** In order to further validate the existence of $MoO_x$ material, the Raman spectroscope is used. The micro-Raman spectra recorded in the wavenumber range, 50–4000 $cm^{-1}$ for different HCl acid concentration is shown in Fig. 11. The micro-Raman peaks for α-$MoO_3$ phase of the sample $S_1$ and $S_2$ are located at ~89, 327, 952 $cm^{-1}$, and 89, 370, 473, 952 $cm^{-1}$, respectively.[57,65,66] In addition, two Raman peaks of h-$MoO_3$ phase are appeared at ~398 and 492 $cm^{-1}$ for the sample $S_1$.[67] The magnified area of the micro-Raman spectra in wavenumber range 50–600 $cm^{-1}$ corresponding to the samples: $S_1$ and $S_2$ are shown in the inset of Fig. 11. Vibrational analysis by micro-Raman spectra reveals that the broad peaks around 1000–600 $cm^{-1}$, 600–200 $cm^{-1}$ and below 200 $cm^{-1}$ are associated with Mo–O stretching, bending and lattice vibration mode, respectively.[66,68] The sharp intense peak located ~89 $cm^{-1}$ is assigned to the rigid transitional vibration of $MoO_4$ tetrahedral chain.[65] The peaks at ~327 and 370 $cm^{-1}$ are assigned to O–Mo–O bending and scissoring vibrations.[57] The characteristics Raman peaks of h-$MoO_3$ phase at ~398 and 492 $cm^{-1}$ are assigned to O–Mo–O vibrational mode.[67] The peak at ~473 $cm^{-1}$ corresponds to the Mo–O stretching and bending vibration of $MoO_6$ octahedra.[69] The presence of $Mo^{6+}$ = O stretching vibration of terminal oxygen atoms is confirmed by the peak at ~952 $cm^{-1}$. These terminal oxygen bonds are created by breaking doubly coordinated oxygen ($Mo_2$–O) bonds at the corner-shared oxygen, which are common to two octrahedra in the α-$MoO_3$ phase.[66] The QDs with mixed phase: α-$MoO_3$ and h-$MoO_3$ transformed to α-$MoO_3$ phase with increase in HCl acid concentration from 25% to 30%. The micro-Raman peaks at ~1645, 3250 and 3425 $cm^{-1}$ are due to $H_2O$ scissor vibration and stretching vibration of the hydrogen-bonded OH groups.[70]

**FTIR characteristics.** The IR absorption spectra of the samples: $S_1$ and $S_2$ shown in Fig. 12, in the wavenumber range 400–4000 $cm^{-1}$ are recorded for further study of vibrational properties of $MoO_x$ QDs. The samples show the absorption peak

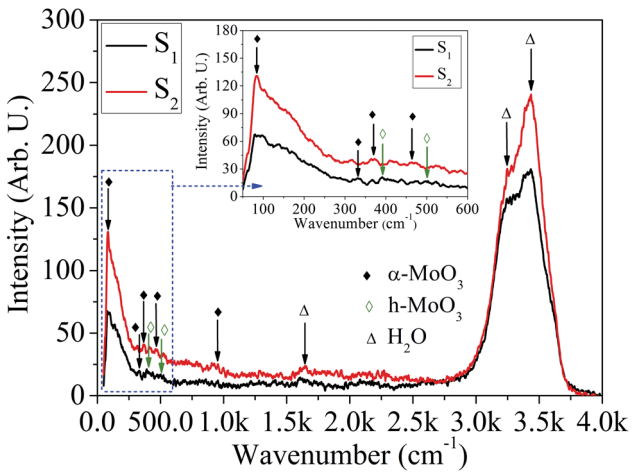


Fig. 11 Micro-Raman spectra of $MoO_x$ QDs for the sample $S_1$ and $S_2$, respectively.

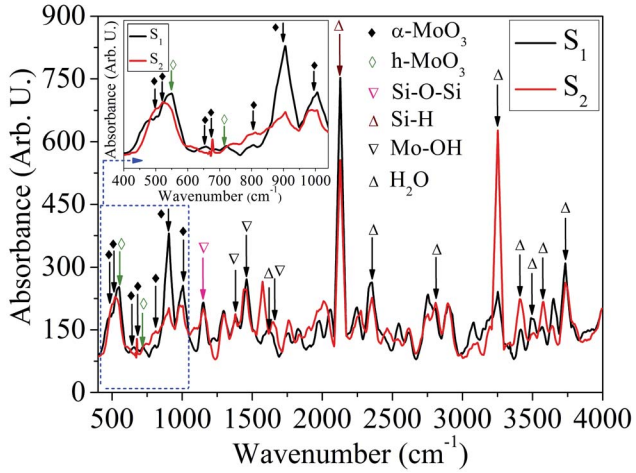


Fig. 12 FTIR absorption spectra of $MoO_x$ QDs for the sample $S_1$ and $S_2$, respectively.

in the spectral range 400–1000 $cm^{-1}$ corresponding to stretching and bending vibrations of metal–oxygen characteristics bonds.[71] The characteristics absorption peaks for α-$MoO_3$ phase of the sample $S_1$ and $S_2$ are located at ~502, 648, 811, 901, 1002 $cm^{-1}$ and ~502, 512, 674, 811, 901, 1002 $cm^{-1}$, respectively.[11,24,40,55,72–74] In addition, two absorption peaks of h-$MoO_3$ phase are appeared at ~548 and 711 $cm^{-1}$ for the sample $S_1$.[67] The magnified area of the FTIR absorption spectra in wavenumber range, 400–1040 $cm^{-1}$ corresponding to the samples: $S_1$ and $S_2$ are shown in the inset of Fig. 12. The absorption peak located at ~502 and 512 $cm^{-1}$ are attributed to the bending mode of vibration of the Mo–O–Mo entity, while the $O^{2-}$ ion is shared by three $Mo^{6+}$ ions.[55,72] The absorption peaks of h-$MoO_3$ phase are ~548 and 711 $cm^{-1}$, associated with the vibration of Mo–O and Mo–O–Mo bond, respectively.[67] The peak at ~648 $cm^{-1}$ could be assigned to the stretching vibration of Mo–O–Mo.[11] The absorption peak at ~674 $cm^{-1}$ is due to the triply coordinated oxygen ($Mo_3$–O) stretching vibrational mode.[40] A broad peak observed at ~811 nm is due to the bridging vibration of Mo=O and indicated that the existence of $Mo^{6+}$ oxidation state is related to the α-$MoO_3$ phase.[73] Two absorption peak located at ~901 and 1002 $cm^{-1}$, associated with the stretching vibration of Mo=O, which is the specification of terminal double bonds. This confirms the basic characterises of a layered structure of α-$MoO_3$.[24,74] The phase transformation of $MoO_x$ ($x$ = 2, 3) QDs with the concentration of HCl acid is also confirmed by FTIR absorption spectra. The peak at ~1157 $cm^{-1}$ is due to Si–O–Si asymmetric vibration in longitudinal optical mode.[75] In addition, three absorption peaks are observed at ~1384, 1460 and 1643 $cm^{-1}$, where first peak is attributed to vibrational mode of the Mo–OH bond and other two correspond to bending mode of Mo–OH, which assigned the presence of adsorbed free water molecules.[59,76] Moreover, the absorption peaks at ~1619, and 3574 $cm^{-1}$ are assigned to the stretching and bending vibration of O–H bonds of adsorbed water molecules, respectively.[77] The peak at ~2110 $cm^{-1}$ corresponds to the stretching vibration of Si–H in dehydrate groups at the silicon surface.[78,79] The absorption peaks located at ~2359, 3245 and 3492 $cm^{-1}$ assigned to the H–O–H bending mode, symmetric and antisymmetric O–H mode of water.[67,80] The absorption peaks at ~2809 and 3400 $cm^{-1}$ are correspond to the typical O–H vibrations due to the adsorbed water molecule on the surface of $MoO_x$ QDs.[40] The peak at ~3737 $cm^{-1}$ associated with the stretching vibration of O–H in silanol groups (Si–OH) isolated by the hydrogen bond.[79] These FTIR results are consistent with the results obtained by HRTEM images and micro-Raman analysis.

## Conclusions

In summary, this work developed a simple and modified top-down approach for synthesis of $MoO_x$ QDs. This process is a combination of thermal evaporation and sonication induced chemical etching to get the desired particles in the solution. The XRD analysis reveals the thermally deposited $MoO_x$ film is amorphous in nature. FETEM image analysis confirms the formation of spherical shaped $MoO_x$ QDs with an average size ~4.3 and 4.6 nm. HRTEM, SAED, micro-Raman, and FTIR analysis reveals that as-prepared QDs exhibit polycrystalline in nature with co-existence of α-$MoO_3$ and h-$MoO_3$ phase. $MoO_x$ QDs exhibited excitation dependent fluorescence emission. The amorphous $MoO_x$ thin film is able to transformed into the polycrystalline nature by this modified top-down approach. The bulk $MoO_3$ powder is successfully transformed to well-dispersed QDs *via* this modified top-down sonication induced chemical etching approach. Further, optimization of various parameters in this approach will lead to the development of tuneable crystal phase and size of the QDs. This work also confirms the successful synthesis of well-dispersed and stable QDs without any surfactants.

## Conflicts of interest

The authors declare no competing financial interest.

## Acknowledgements

This work is partially supported by the UGC-BSR research project no. F.30-10/2017(BSR) and DST FIST grant (project no. SR/FST/PSI-217/2016) to the Department of Physics, Dibrugarh University, Dibrugarh. The authors acknowledge the CIF, IIT Guwahati, India, for providing the FETEM, FTIR, and Laser micro-Raman facilities.

## References

1 H. Cheng, T. Kamegawa, K. Mori and H. Yamashita, *Angew. Chem.*, 2014, **53**, 2910–2914.
2 D. Hanlon, C. Backes, T. Higgins, M. Hughes, A. O. Neill, P. King, N. Mcevoy, G. Duesberg, B. Sanchez and H. Pettersson, *Chem. Mater.*, 2014, **26**, 1751–1763.
3 M. Ibrahem, F. Wu, D. Mengistie, C. Chang, L. Li and C. Chu, *Nanoscale*, 2014, **6**, 5484–5490.
4 B. Gao, H. Fan and X. Zhang, *J. Phys. Chem. Solids*, 2012, **73**, 423–429.
5 L. Wang, X. Zhang, Y. Ma, M. Yang and Y. Qi, *Mater. Lett.*, 2016, **164**, 623–626.
6 B. Hu, L. Mai, W. Chen and F. Yang, *ACS Nano*, 2009, **3**, 478–482.
7 J. Zhou, N. S. Xu, S. Z. Deng, J. Chen, J. C. She and Z. L. Wang, *Adv. Mater.*, 2003, **15**(21), 1835.
8 I. Shakir, M. Shahid, U. A. Rana and M. F. Warsi, *RSC Adv.*, 2014, **4**, 8741–8745.
9 G. Wei, W. Qin, D. Zhang, G. Wang, R. Kim, K. Zheng and L. Wang, *J. Alloys Compd.*, 2009, **481**, 417–421.
10 M. Wang and K. J. Koski, *ACS Nano*, 2015, **9**, 3226–3233.
11 G. Song, J. Shen, F. Jiang, R. Hu, W. Li, L. An, R. Zou, Z. Chen, Z. Qin and J. Hu, *ACS Appl. Mater. Interfaces*, 2014, **6**, 3915–3922.
12 J. Yang, F. Lu, Y. Li, S. Yang, R. Li, N. Huo, C. Fan, Z. Wei, J. Li and S. S. Li, *J. Mater. Chem. C*, 2014, **2**(6), 1034–1040.
13 S. S. Sunu, E. Prabhu, V. Jayaraman, K. I. Gnanasekar and T. Gnanasekaran, *Sens. Actuators, B*, 2003, **94**, 189–196.

 

14 F. J. Zhang, D. W. Zhao, Z. L. Zhuo, H. Wang, Z. Xu and Y. S. Wang, *Sol. Energy Mater. Sol. Cells*, 2010, **94**, 2416–2421.
15 M. Y. Ameen, S. Pradhan, M. R. Suresh and V. S. Reddy, *Opt. Mater.*, 2015, **39**, 134–139.
16 L. Zhou, L. Yang, P. Yuan, J. Zou, Y. Wu and C. Yu, *J. Phys. Chem. C*, 2010, **114**, 21868–21872.
17 A. M. Hashem, H. Groult, A. Mauger, K. Zaghib and C. M. Julien, *J. Power Sources*, 2012, **219**, 126–132.
18 S. Balendhran, S. Walia, M. Alsaif, E. P. Nguyen, J. Z. Ou, S. Zhuiykov, S. Sriram, M. Bhaskaran and K. Kalantar-zadeh, *ACS Nano*, 2013, **7**, 9753–9760.
19 S. Bai, S. Chen, L. Chen, K. Zhang, R. Luo, D. Li and C. C. Liu, *Sens. Actuators, B*, 2012, **174**, 51–58.
20 T. A. Tran, K. Krishnamoorthy, Y. W. Song, S. K. Cho and S. J. Kim, *ACS Appl. Mater. Interfaces*, 2014, **6**, 2980–2986.
21 K. Krishnamoorthy, M. Premanathan, M. Veerapandian and S. J. Kim, *Nanotechnology*, 2014, **25**, 315101.
22 X. Lu, R. Wang, F. Yang, W. Jiao, W. Liu, L. Hao and X. Hea, *J. Mater. Chem. C*, 2016, **4**(28), 6720–6726.
23 Y. Xu, X. Wang, W. L. Zhang, F. Lv and S. Guo, *Chem. Soc. Rev.*, 2018, **47**, 586–625.
24 L. Yuan, Y. Niu, R. Li, L. Zheng, Y. Wang, M. Liu, G. Xu, L. Huang and Y. Xu, *J. Mater. Chem. B*, 2018, **6**(20), 3240–3245.
25 L. Zhang, M. F. Hong, Z. J. Chu, H. Xu, S. P. Wang, X. J. Zhao and S. J. Xiao, *Microchem. J.*, 2018, **141**, 170–175.
26 H. Zu, Y. Guo, H. Yang, D. Huang, Z. Liu, Y. Liu and C. Hu, *New J. Chem.*, 2018, **42**, 18533–18540.
27 B. Li, X. Wang, X. Wu, G. He, R. Xu, X. Lu, F. R. Wang and I. P. Parkin, *Nanoscale*, 2017, **9**(31), 11012–11016.
28 T. T. P. Pham, P. H. D. Nguyen, T. T. Vo, H. H. P. Nguyen and C. L. Luu, *Adv. Nat. Sci.: Nanosci. Nanotechnol.*, 2015, **6**, 045010.
29 Q. Xu, W. Cai, W. Li, T. S. Sreeprasad, Z. He, W. J. Ong and N. Li, *Mater. Today Energy*, 2018, **10**, 222–240.
30 L. Niu, J. N. Coleman, H. Zhang, H. Shin, M. Chhowalla and Z. Zheng, *Small*, 2016, **12**, 272–293.
31 X. Zhang, Z. Lai, Z. Liu, C. Tan, Y. Huang, B. Li, M. Zhao, L. Xie, W. Huang and H. Zhang, *Angew. Chem., Int. Ed.*, 2015, **54**(18), 5425–5428.
32 Y. P. Sun, B. Zhou, Y. Lin, W. Wang, K. A. S. Fernando, P. Pathak, M. J. Meziani, B. A. Harruff, X. Wang, H. Wang, P. G. Luo, H. Yang, M. E. Kose, B. Chen, L. M. Veca and S. Y. Xie, *J. Am. Chem. Soc.*, 2006, **128**, 7756–7757.
33 L. A. Ponomarenko, F. Schedin, M. I. Katsnelson, R. Yang, E. W. Hill, K. S. Novoselov and A. K. Geim, *Science*, 2008, **320**, 356–358.
34 Q. Huang, S. Hu, J. Zhuang and X. Wang, *Chem.–Eur. J.*, 2012, **18**(48), 15283–15287.
35 S. Xu, D. Li and P. Wu, *Adv. Funct. Mater.*, 2015, **25**(7), 1127–1136.
36 D. Gopalakrishnan, D. Damien and M. M. Shaijumon, *ACS Nano*, 2014, **8**(5), 5297–5303.
37 Z. Sun, H. Xie, S. Tang, X. F. Yu, Z. Guo, J. Shao, H. Zhang, H. Huang, H. Wang and P. K. Chu, *Angew. Chem., Int. Ed.*, 2015, 11526–11530.
38 Z. Wu, D. Wang, X. Liang and A. Sun, *Ultrason. Sonochem.*, 2011, **18**, 288–292.
39 D. J. Borah, A. T. T. Mostako, P. K. Saikia and P. Dutta, *Mater. Sci. Semicond. Process.*, 2019, **93**, 111–122.
40 N. Wang, D. Tang, H. Zou, S. Jia, Z. Sun, X. Yang and J. Peng, *Opt. Mater.*, 2018, **83**, 19–27.
41 H. S. Dehsari, A. H. Ribeiro, B. Ersoz, W. Tremel, G. Jakob and K. Asadi, *CrystEngComm*, 2017, **19**(44), 6694–6702.
42 J. H. Huang, H. J. Parab, R. S. Liu, T. C. Lai, M. Hsiao, C. H. Chen, H. S. Sheu, J. M. Chen, D. P. Tsai and Y. K. Hwu, *J. Phys. Chem. C*, 2008, **112**, 15684–15690.
43 L. Jiwen, W. Shizhong, Z. Guo-shang, X. Liujie, L. Wei and P. Kunming, *Int. J. Electrochem. Sci.*, 2017, **12**, 2429–2440.
44 Y. P. Fang, A. W. Xu, A. M. Qin and R. J. Yu, *Cryst. Growth Des.*, 2005, **5**(3), 1212–1225.
45 T. Xia, Q. Li, X. Liu, J. Meng and X. Cao, *J. Phys. Chem. B*, 2006, **110**, 2006–2012.
46 Y. Zhang, H. Zhang, M. Ma, X. Guo and H. Wang, *Appl. Surf. Sci.*, 2009, **255**, 4747–4753.
47 C. M. Donega, S. G. Hickey, S. F. Wuister, D. Vanmaekelbergh and A. Meijerink, *J. Phys. Chem. B*, 2003, **107**(2), 489–496.
48 Y. Zhan, Y. Liu, H. Zu, Y. Guo, S. Wu, H. Yang, Z. Liu, B. Lei, J. Zhuang, X. Zhang, D. Huang and C. Hu, *Nanoscale*, 2018, **10**(13), 5997–6004.
49 I. A. Castro, R. S. Datta, J. Z. Ou, A. C. Gomez, S. Sriram, T. Daeneke and K. K. Zadeh, *Adv. Mater.*, 2017, **29**(40), 1701619.
50 P. A. Arasu and R. V. Williams, *J. Adv. Dielectr.*, 2017, **7**, 1750011.
51 J. Tauc, *Mater. Res. Bull.*, 1968, **3**, 37–46.
52 I. Navas, R. Vinodkumar and V. P. M. Pillai, *Appl. Phys. A*, 2011, **103**, 373–380.
53 S. Sapra and D. D. Sarma, *Phys. Rev. B: Condens. Matter Mater. Phys.*, 2004, **69**, 125304.
54 A. H. Hammad and M. S. Abdel-wahab, *Optik*, 2018, **154**, 777–784.
55 R. K. Sharma and G. B. Reddy, *J. Alloys Compd.*, 2014, **598**, 177–183.
56 A. Boukhachem, C. Bouzidi, R. Boughalmi, R. Ouerteni, M. Kahlaoui, B. Ouni, H. Elhouichet and M. Amlouk, *Ceram. Int.*, 2014, **40**, 13427–13435.
57 F. Chandoul, A. Boukhachem, F. Hosni, H. Moussa, M. S. Fayache, M. Amlouk and R. Schneider, *Ceram. Int.*, 2018, **44**(11), 12483–12490.
58 A. Boukhachem, M. Mokhtari, N. Benameur, A. Ziouche, M. Martínez, P. Petkova, M. Ghamnia, A. Cobo, M. Zergoug and M. Amlouk, *Sens. Actuators, A*, 2017, **253**, 198–209.
59 A. Klinbumrung, T. Thongtem and S. Thongtem, *J. Nanomater.*, 2012, **2012**, 1–5.
60 S. J. Xiao, X. J. Zhao, Z. J. Chu, H. Xu, G. Q. Liu, C. Z. Huang and L. Zhang, *ACS Omega*, 2017, **2**(4), 1666–1671.
61 S. J. Xiao, X. J. Zhao, P. P. Hu, Z. J. Chu, C. Z. Huang and L. Zhang, *ACS Appl. Mater. Interfaces*, 2016, **8**, 8184–8191.
62 S. J. Xiao, X. J. Zhao, J. Zuo, H. Q. Huang and L. Zhang, *Anal. Chim. Acta*, 2016, **906**, 148–155.

63 X. Wang, G. Sun, N. Li and P. Chen, *Chem. Soc. Rev.*, 2016, **45**(8), 2239–2262.
64 J. Zhang, Y. Pan, Y. Chen and H. Lu, *J. Mater. Chem. C*, 2018, **6**(9), 2216–2220.
65 M. Dieterle, G. Weinberg and G. Mestl, *Phys. Chem. Chem. Phys.*, 2002, **4**, 812–821.
66 I. Navas, R. Vinodkumar, K. J. Lethy, A. P. Detty, V. Ganesan, V. Sathe and V. P. M. Pillai, *J. Phys. D: Appl. Phys.*, 2009, **42**, 175305.
67 V. V. Atuchin, T. A. Gavrilova, V. G. Kostrovsky, L. D. Pokrovsky and I. B. Troitskaia, *Inorg. Mater.*, 2008, **44**, 622–627.
68 Y. Chen, C. Lu, L. Xu, Y. Ma, W. Hou and J. J. Zhu, *CrystEngComm*, 2010, **12**, 3740–3747.
69 Y. L. Xie, F. C. Cheong, Y. W. Zhu, B. Varghese, R. Tamang, A. A. Bettiol and C. H. Sow, *J. Phys. Chem. C*, 2010, **114**, 120–124.
70 I. Pernoll, U. Maier, R. Janoschek and G. Zundel, *J. Chem. Soc., Faraday Trans. 2*, 1975, **71**(10), 201–206.
71 A. Chithambararaj and A. C. Bose, *J. Alloys Compd.*, 2011, **509**, 8105–8110.
72 J. Chen, M. Wang, X. Liao, Z. Liu, J. Zhang, L. Ding, L. Gao and Y. Li, *J. Alloys Compd.*, 2015, **619**, 406–410.
73 S. Subbarayudu, V. Madhavi and S. Uthanna, *ISRN Condens. Matter Phys.*, 2013, **2013**, 1–9.
74 V. Nirupama, K. R. Gunasekhar, B. Sreedhar and S. Uthanna, *Curr. Appl. Phys.*, 2010, **10**, 272–278.
75 R. A. Oweini and H. E. Rassy, *J. Mol. Struct.*, 2009, **919**, 140–145.
76 R. K. Sharma and G. B. Reddy, *Phys. B*, 2015, **456**, 197–205.
77 P. Wongkrua, T. Thongtem and S. Thongtem, *J. Nanomater.*, 2013, **2013**, 1–8.
78 Y. J. Chabal, *Surf. Sci.*, 1986, **168**, 594–608.
79 A. G. Milekhin, C. Himcinschi, M. Friedrich, K. Hiller, M. Wiemer, T. Gessner, S. Schulze and D. R. T. Zhan, *Semiconductors*, 2006, **40**, 1304–1313.
80 B. Gowtham, V. Ponnuswamy, G. Pradeesh, J. Chandrasekaran and D. Aradhana, *J. Mater. Sci.: Mater. Electron.*, 2018, **29**, 6835–6843.

 